


## PAPER

View Article Online  
View Journal | View Issue



Cite this: *Energy Environ. Sci.*, 2024, 17, 2864

# Three-dimensional electrode characteristics and size/shape flexibility of coaxial-fibers bundled batteries†

Yoshinari Makimura,  \* Chikaaki Okuda, Toshihisa Munekata, Azusa Tsukigase, Hideaki Oka, Tooru Saeki, Ryohei Morimoto, Megumi Sasaki, Hiroyuki Nakano, Yuichi Ito, Mamoru Mizutani and Tsuyoshi Sasaki

Future energy storage applications emerging from technological innovations, such as drones and smart devices, require batteries to be small and slender while maintaining high energy density and power capability, fast charging, long cycling/calendar life, and safety. In this study, coaxial-fibers bundled batteries (CFBBs) are proposed, wherein the center is a negative electrode made of carbon fibers, the inner shell is a separator made of  $\text{Al}_2\text{O}_3$  and polyvinylidene fluoride (PVDF), and the outer shell is a positive electrode. These batteries have flexibility in size and shape by changing the number of bundled electrodes. A 225 mA h CFBB consisting of 288 fiber-electrodes exhibited a high-rate capability of 180 mA h at a 7.6C-rate and a capacity retention of 92% after 100 cycles without marked degradation. A 3.3 mA h CFBB consisting of four fiber-electrodes exhibited 90% capacity retention after 100 cycles. Electrochemical–thermal coupled simulations of CFBBs predicted high safety in the event of an internal short-circuit, and the nail penetration test on the 225 mA h CFBB at 4.2 V demonstrated that the temperature rise was limited to 48 °C by the characteristic safety mechanism. Manufacturing processes to enable mass production are described and a flight test of a drone with four 225 mA h CFBBs is conducted to demonstrate their performance. A flexure test of the CFBBs consisting of 288 fiber-electrodes demonstrated that CFBBs have sufficiently high strength to be applied as the frameworks of drones and wearable devices and as their power sources.

Received 18th January 2024,  
Accepted 15th March 2024

DOI: 10.1039/d4ee00283k

rsc.li/ees

## Broader context

The rise in demands for electrified vehicles and stationary energy storage to overcome environmental issues has driven the rapid expansion of applications ranging from mobile batteries to large battery packs. Batteries must achieve higher performance in terms of energy density, power capability, fast charging, cycling/calendar life, and safety, while the trade-off relations between these performances need to be controlled in the present batteries. In this paper, coaxial-fibers bundled batteries (CFBBs) with a novel 3D electrode architecture are proposed to provide fundamental solutions for the trade-off relations. The 3D electrode structure of CFBBs is preferred from the manufacturing process perspective since the coaxial 3D electrode structure is made by layering a separator and positive electrode on the surface of the cylindrical carbon fiber unit. The coaxial-fiber structure increases the electrode-facing area and shortens the ionic conduction pathway in the electrodes, leading to the compatibility of rapid charge–discharge capability with high energy density. The carbon fiber serves as a current collector without copper foil, contributing to increased energy density and eliminating the resource scarcity risk of copper. CFBBs have the size/shape flexibility and strength equivalent to glass-fiber-reinforced plastics. Characteristic features of CFBBs allow them to be used as frameworks and power sources for the future applications.

Toyota Central R&D Labs., Inc, Nagakute, Aichi 480-1192, Japan. E-mail: ymakimura@mosk.tytlabs.co.jp

† Electronic supplementary information (ESI) available: Schematic illustrations of 3D electrode structures, voltage profiles of the carbon fiber unit, viscosity of the slurries used for the electrodes or separator coating as a function of the shear rate, cross-sectional images of a single coaxial-fiber electrode, simulated temperature distribution of the fiber-bundled structure, rate capability and the nail penetration test of the sandwich-type multi-sheet battery, the experimental setup of the nail penetration test, rate capability of the CFBBs consisting of 72 or 6 fiber electrodes and of 36 fiber electrodes with high energy-density and increased capacity, capacity retention of the CFBB consisting of 4 fiber electrodes, the video of a test flight of a drone with four CFBBs, electrode and battery-design parameters, the sizes with standard deviation  $\sigma$  of each component in a single coaxial-fiber electrode, the size, weight, and energy density of the CFBBs, energy densities and high-rate capabilities of the commercial lithium-ion batteries, estimated Joule heat and temperature rise of carbon fibers during high-rate discharge, and charge and discharge currents and the C-rates from the rate-capability tests of CFBBs. See DOI: <https://doi.org/10.1039/d4ee00283k>



## Introduction

Technological innovation in mobile electronic devices is closely related to the downsizing of lithium-ion batteries (LIBs) by enhancing their energy density. Over the past 30 years, LIBs have evolved to exhibit the highest practicable energy density.<sup>1</sup> To overcome urgent environmental challenges, the rise in demands for electrified vehicles and stationary energy storage has driven the rapid expansion of applications ranging from mobile batteries to large battery packs.<sup>2–4</sup> In line with the diverse applications of LIBs, batteries must achieve higher performance with respect to energy density, power capability, fast charging, cycling/calendar life, and safety.

In LIBs, a sandwich-type internal structure consisting of positive and negative electrodes separated by a polyethylene membrane is wound or stacked and tightly sealed after electrolyte-filling in a cylindrical, prismatic, or pouch cell.<sup>5</sup> For the sandwich-type structure shown in Fig. S1(a) (ESI<sup>†</sup>), the electrodes must be thick and dense to achieve high energy density. The electrodes increase resistance due to the clogged ionic conduction pathway in the porous electrode, leading to low power density and slow charging. This sandwich-type structure provides a trade-off between energy density and rapid charge-discharge capabilities. Sandwich-type LIBs have the safety mechanisms of separator shutdown, which shuts off the current flow by closing the separator holes due to heat generation, and a safety valve on a cylindrical or prismatic cell, which shuts off the current flow by opening the valve due to gases generated in the battery.

Research on electrode materials has been extensively conducted worldwide to overcome the trade-off. LiNiO<sub>2</sub>-derivatives have been developed for practical applications as positive-electrode materials,<sup>6–12</sup> and the search for new materials is active.<sup>13–21</sup> Metal/alloy electrodes, such as silicon and lithium metal, have been extensively examined to increase their energy density as negative-electrode materials.<sup>22–24</sup> To find another fundamental solution, innovative three-dimensional (3D) electrode structures are preferred due to their high energy density and large electrode area, leading to rapid charge-discharge capability. 3D porous tri-continuous structures composed of positive and negative electrodes isolated by separators have been proposed to accelerate the electrochemical reaction.<sup>25,26</sup>

For classical battery-package forms, the size, shape, and rigidity of the battery limit the design of devices and this trend will be even more pronounced with the rise of future technologies such as smart or wearable devices. Fiber, cable, and wire-shaped 3D electrode structures have been proposed as batteries with flexibility, weavability, and stretchability<sup>27–33</sup> and the performance of fiber-shaped batteries has been demonstrated by several researchers by lighting a light-emitting diode (LED) lamp or screen.<sup>27–29,31–33</sup> The 3D electrode structure that does not have a porous membrane as a separator requires safety mechanisms other than separator shutdown. Safety mechanisms unique to the 3D electrode structure are desirable. In addition to the structural features of the small size and slender shape of the battery, the increased strength of the 3D

electrode structure makes it possible to apply the batteries as the frameworks of devices.<sup>34</sup> With 3D electrode structures, the shapes of devices will no longer be limited by the size and shape of the batteries, thereby enabling unique device designs.

In this paper, we propose coaxial-fibers bundled batteries (CFBBs), which have a new 3D electrode architecture and are expected to have high energy densities, high power capability, fast charging, long cycling life, and safety, and they can be freely scaled in size and shape by changing the number of coaxial-fiber electrodes to be bundled. Flight tests of a drone with the batteries are performed to demonstrate the performance of the batteries and the mechanical properties of CFBBs are examined with the aim of applying them as the frameworks of devices. A coaxial fiber structure is preferred for battery manufacturing and newly developed manufacturing processes that enable mass production of CFBBs are proposed.

## Results and discussion

### Basic design and parametric study of CFBBs

In a battery with a sandwich-type structure shown in Fig. S1(a) (ESI<sup>†</sup>), the positive and negative electrodes face each other with a separator between them, and the current collectors are positioned on the electrodes on the opposite side of the separator. To increase the electrode-facing area, a grid pattern, shown in Fig. S1(b) (ESI<sup>†</sup>), was devised, known as the 3D-electrode structure. In this structure, the electrodes are made into rods so that they face each other on four sides. The 3D grid pattern of the rods increases the electrode surface area and shortens the ionic-conduction pathway; however, it is difficult to arrange the positive and negative electrode rods alternately without misalignment in terms of both the reproducibility of the electrode structure and the construction of manufacturing processes. Thus, this study proposed a new 3D coaxial-fiber structure that does not suffer from these problems. The proposed structure is shown in Fig. S1(c) (ESI<sup>†</sup>). The coaxial-fiber structure further increases the electrode surface area and shortens the ionic conduction pathway. Fig. 1(a) displays a schematic illustration of a single coaxial-fiber battery in which the cylindrical center is a negative electrode made of a carbon fiber unit, the inner shell is a separator made of Al<sub>2</sub>O<sub>3</sub>-particles with PVDF, and the outer shell is a positive electrode.<sup>35</sup> A coaxial-fiber structure is preferred from a manufacturing perspective since the structure has a layered separator and positive electrode on the surface of the cylindrical carbon fiber unit. The illustration shown in Fig. 1(a) is simplified to gain a better understanding of the coaxial-fiber structure.

The fabricated battery has a multilayer coating to prevent a short circuit between positive and negative electrodes. Fig. 1(b) shows the energy density and surface area between the positive and negative electrodes of a single coaxial-fiber structure as a function of the average radius of the carbon fiber unit; the energy density and surface area between the positive and negative electrodes of a conventional sandwich-type structure as a function of the negative electrode thickness are also shown



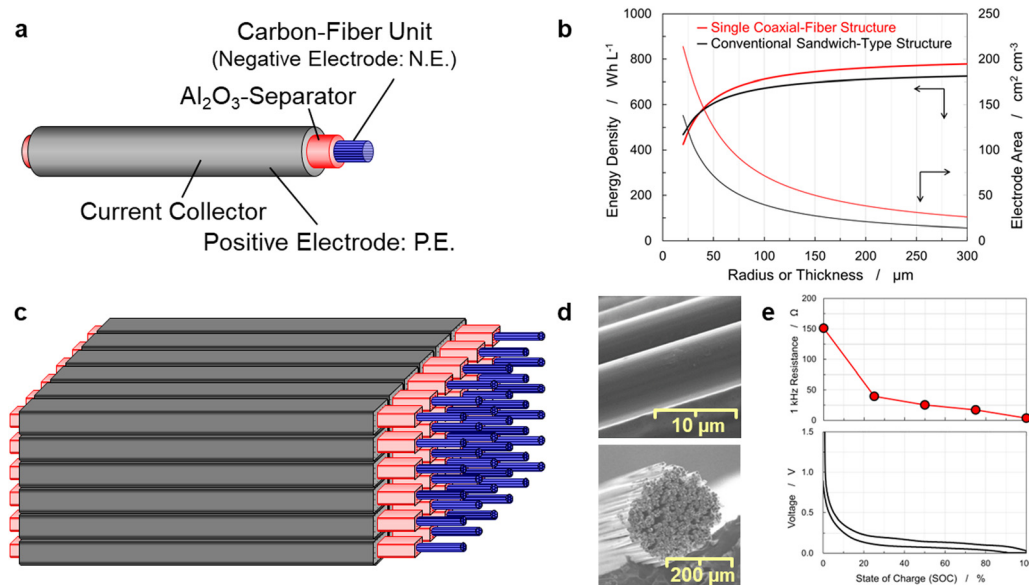


**Fig. 1** Schematic illustration of a coaxial-fibers bundled battery (CFBB) and electrochemical characterization of the carbon fiber unit. (a) Single coaxial-fiber cell consisting of a carbon fiber unit of the negative electrode, which serves as the core material, and a positive electrode placed in the shell of the cell. Positive and negative electrodes were separated by  $\text{Al}_2\text{O}_3$ -particles with polyvinylidene fluoride (PVDF). (b) Energy densities and electrode areas as a function of the thickness of the negative electrode. The electrode areas are proportional to the rate capability. The results of CFBBs are compared with those of a conventional sandwich-type multi-sheet battery in which positive and negative electrode sheets are stacked alternately. The thickness of the negative electrode in CFBBs corresponds to the radius of the carbon fiber unit. (c) CFBB fabricated by bundling coaxial-fiber electrodes. (d) Scanning electrode microscopy (SEM) images of the carbon fiber unit. (e) Voltage profiles of the carbon fiber unit of 210 mm length with lithium metal sheets of 200 mm length in the pouch cell displayed in Fig. S2(a) (ESI<sup>†</sup>). The states of charge were calculated from the capacity by considering the fully charged state at 0.005 V as 100%. The change in resistance at 1 kHz between two electrode tabs at both sides of the carbon fiber unit is measured as a function of the state of charges (SOCs).

for comparison. The electrode areas were proportional to the rate capability. The electrode and battery design parameters of the model structure are listed in Table S1 (ESI<sup>†</sup>). The discharge capacity of the carbon fiber is  $330 \text{ mA h g}^{-1}$ , which is comparable to that of the graphite negative-electrode.<sup>36,37</sup> The coaxial fiber structure exhibited a higher energy density than a conventional sandwich-type structure at the same electrode thickness. With regard to the conditions under which both electrodes had the same energy density, the coaxial-fiber structure could not only maintain a short ionic-conduction pathway, but also increase the electrode surface area. These structural features of the electrodes suggest that the rapid charge-discharge capability of the coaxial-fiber structure is compatible with high energy density.

Fig. 1(c) shows a schematic of a CFBB. In this CFBB, long carbon fibers were applied as a negative electrode instead of a porous sheet of powdered graphite. The carbon fiber itself can serve as a current collector without copper foil, therefore contributing to increased energy density and eliminating the resource scarcity risk of copper.<sup>38</sup> To fabricate the designed structure, it is important to understand the charge-discharge characteristics of carbon fiber and the changes in physical properties during battery operation.

### Carbon-fiber unit

SEM images of the carbon fiber surfaces and their cross-sections are shown in Fig. 1(d). The round-shaped carbon fiber unit with  $\sim 250 \text{ } \mu\text{m}$  diameter was prepared by bundling and

twisting 400 carbon fibers (a diameter of approximately  $7 \text{ } \mu\text{m}$ ) with poly[vinylidene fluoride-co-hexafluoropropylene] (P(VDF/HFP)). Four hundred was selected as the optimal number as when fewer than 400 carbon fibers were used, they were more likely to break during processing. In contrast, as the number of carbon fibers increased above 400, the radius of the carbon fiber unit increased and the surface area decreased significantly based on the relationship between the radius and the energy density or surface area shown in Fig. 1(b). Fig. S2(a) (ESI<sup>†</sup>) shows the pouch-type electrochemical cell used to examine the carbon fiber unit. The carbon fiber unit exhibited a discharge capacity of  $256 \text{ mA h g}^{-1}$  and could be reversibly operated as an electrode material. As CFBBs do not use copper current collectors, it is important to maintain low electrical resistivity in the batteries. The graphite negative-electrode was reported to exhibit approximately  $0.04 \text{ } \Omega \text{ cm}$  electrical resistivity,<sup>39,40</sup> whereas the carbon fiber unit exhibited  $3.4 \times 10^{-3} \text{ } \Omega \text{ cm}$ , which is an order of magnitude lower. The electrical resistivity of the current collector, a copper sheet of  $10 \text{ } \mu\text{m}$  thickness, was calculated to be  $1.68 \times 10^{-6} \text{ } \Omega \text{ cm}$ .<sup>41</sup> The electrical resistivity of the carbon fiber unit was sufficiently low to generate a large electric current. In batteries, lithium ions are intercalated into carbon fibers, and the unit must maintain sufficient electrical resistance, even in the charged state. To examine the electrical resistance of the carbon fiber unit upon lithium-intercalation, an electrochemical cell of a single 210 mm long carbon fiber unit with a 200 mm long lithium-metal sheet was fabricated. After charge-discharge was



performed at a C/10-rate for 3 cycles, the resistance between both ends of the carbon fiber unit was measured at 1 kHz at differently charged states, where the fully charged state was defined as 100% of the state of charge (SOC). The resistance at 1 kHz at selected SOC and the voltage profile are displayed in Fig. 1(e). The carbon fiber unit exhibited 151  $\Omega$  in the discharged state for SOC 0%, which was comparable to 73  $\Omega$ , as estimated from  $3.4 \times 10^{-3} \Omega \text{ cm}$  volume resistivity. Moreover, the electrical resistance of the carbon fiber unit decreased with charging. This implies that a carbon fiber unit exhibits high electrical conductivity, especially in charged states, and therefore excellent battery performance, which can be expected even without a copper current collector.

As shown in Fig. S2(b) (ESI<sup>†</sup>), the carbon fiber unit exhibited an operating voltage of approximately 0.1 V, which is similar to that of the graphite negative-electrode,<sup>42</sup> and the voltage profile had a slope of 0.2–1.0 V. The discharge capacity of 256  $\text{mA h g}^{-1}$  and a partially sloping voltage profile are the characteristics of moderately graphitized carbon materials.<sup>43</sup> Doubling the number of fibers in the carbon fiber unit reduced the discharge capacity at the 4C-rate to about 65%. Pitch-based carbon fiber with relatively high graphitization was selected from commercially available materials to achieve high capacity and high electrical conductivity simultaneously. Four hundred filaments of the pitch-based carbon fiber of approximately 7  $\mu\text{m}$  in diameter were formed into a yarn (Nippon Graphite Fiber Corporation, Japan), which was used as a negative electrode for the CFBB. The carbon fiber used in this paper has a tensile strength of 3530 MPa, a Young's modulus of 800 GPa, and a volume resistivity of  $3.4 \times 10^{-3} \Omega \text{ cm}$ . The improvement of carbon fibers is expected to combine a higher degree of graphitization and sufficient flexibility to contribute to higher capacity for CFBB applications.

### Fabrication of CFBBs

Fig. 2 shows the manufacturing processes of the proposed CFBBs, which consist of twisting carbon fibers, coating the

separator and electrode slurry, cutting coaxial-fiber electrodes, stripping the positive electrode and separator on the fiber surface with a laser, vertical/horizontal two-way pressing, packaging, and electrolyte-filling. To fabricate coaxial-fiber electrodes, the electrode sizes have to be controllable, and the electrode structure has to be reproducible with the determined parameters. Since the coaxial-fiber structure is fabricated using slurry coatings, it is important that there is no short circuit between the positive and negative electrodes during fabrication processes and charge/discharge operations. The following three points are important for the fabrication of the coaxial-fiber electrodes in a stable and reproducible manner: first, the surface of the cylindrical carbon fiber unit should be smooth to form a coaxial-fiber structure by coating and drying the slurries of the separator and positive electrode in sequence on the cylindrical surfaces; second, mixing of the particles used in the separator and electrodes must be avoided during coating and the formation of cracks or micropores must be avoided during coating and battery operation; third, it is important to form electrode interphases with low charge transfer resistance in the coaxial-fiber electrodes and internal microstructures that allow lithium ions to move smoothly within the electrodes and separator. The processes to fabricate the coaxial-fiber electrode were constructed to ensure the three key points described above.

Fig. 3(a) displays the coating machine and setup to prepare the coaxial-fiber structure, which consists of a coating nozzle, heater, and two spools with/without carbon fiber. Carbon fiber filaments pulled from the spool at the top of the coating machine were passed through a coating nozzle with P(VDF/HFP) dissolved in *N*-methyl-2-pyrrolidone (NMP) and heaters and then connected to an empty spool at the bottom. The spool at the top rotated to twist the fibers tightly and densify them.

Magnified images of the nozzle and shape of the electrode during the coating processes are shown in Fig. 3(b). The 400 carbon fiber filaments wound on the spool had a flat shape. During the coating process, the filaments with P(VDF/HFP) are bundled and twisted to form a cylindrical shape. P(VDF/HFP)

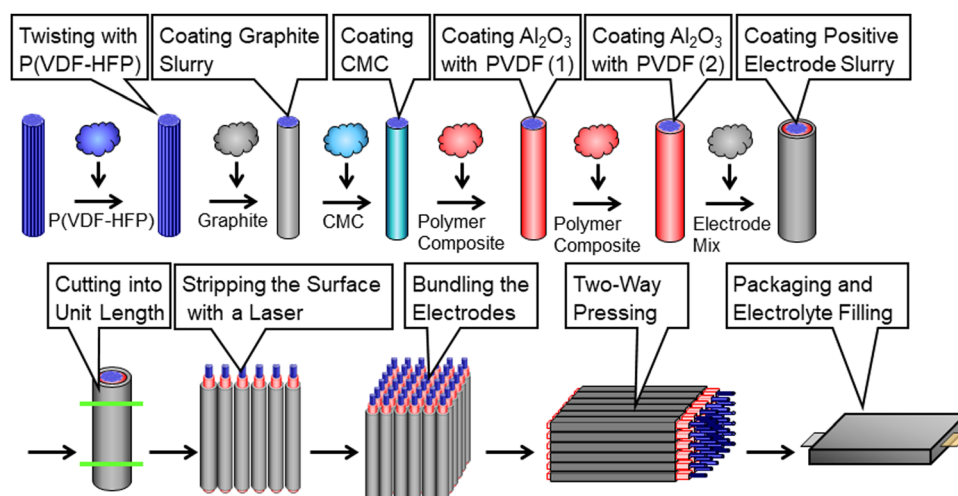
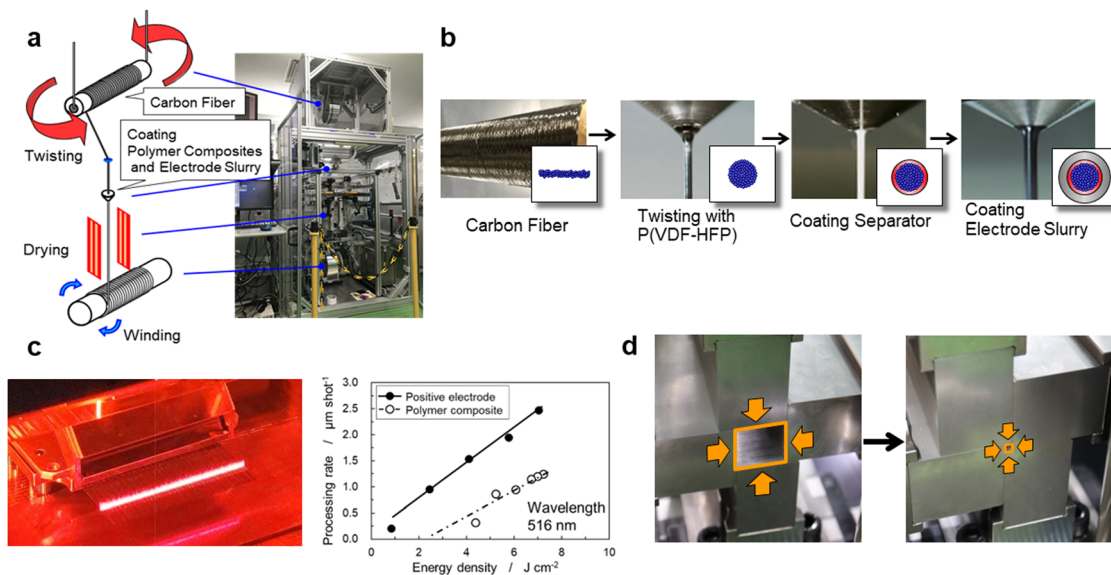


Fig. 2 Schematic illustration of the processes to fabricate CFBBs.







**Fig. 3** Manufacturing processes of coaxial-fibers bundled battery (CFBB) fabrication. (a) Photograph and the setup to prepare the coaxial-fiber electrode by twisting carbon fibers in a coating polymer and then the positive electrode slurry. (b) Magnified images of the coating nozzle and the shape of the electrode as the process progresses. (c) Laser processing method using the wavelength of 516 nm to strip the coating surface from the carbon fiber unit. (d) Photograph of the vertical/horizontal two-way pressing method to compress and densify the coaxial-fiber electrode.

was used instead of PVDF for the preparation of the cylindrical carbon fiber unit to prevent the increase in the charge transfer resistance of the negative electrode owing to P(VDF/HFP) acting as a gel polymer electrolyte inside the carbon fiber unit after the electrolyte was filled to form the battery. To smooth the bumpy surface of the carbon-fiber unit, an electrode slurry of graphite, which has about 5  $\mu\text{m}$  of the particle size, was coated on the carbon fiber unit. When an aqueous slurry with carboxymethyl cellulose (CMC) and the styrene-butadiene rubber (SBR) binder was used for graphite coating, the surface of the cylindrical carbon fiber unit was bumpy and unstable. The slurry of graphite with PVDF dissolved in NMP was, therefore, used to smooth the surface of the cylindrical negative electrode. When slurries are coated on cylindrical surfaces with small diameters, the coated layer may form bumpy surfaces owing to Plateau-Rayleigh instability caused by the effect of the surface tension of the slurry.<sup>44–46</sup> To make the coated layers uniform and stable, the coating process needs to be adapted to the slurry viscosity during and after coating. Fig. S3 (ESI<sup>†</sup>) displays the change in viscosity for the slurries used for the electrodes or separator coating as a function of the shear rate to fabricate the coaxial-fiber structure. In terms of the coating speed of the slurries, the viscosity during coating should have a shear rate of approximately  $1000\text{ s}^{-1}$  or that after coating or before drying should have a shear rate of approximately  $0.1\text{ s}^{-1}$  in the coated layer. The viscosity of the slurries below  $1000\text{ mPa s}$  is suitable for smooth and stable coating without steps or streaks during slurry-coating but high viscosity is preferred after coating to maintain uniform layers and smooth surfaces without the formation of cracks or micropores. The slurry of graphite with PVDF dissolved in NMP exhibits shear-thinning behavior, where viscosity becomes lower at a higher shear rate, as shown

in Fig. S3 (ESI<sup>†</sup>), since the slurry belongs to pseudoplastic fluid. Even when the viscosity of solids is adjusted to be below  $1000\text{ mPa s}$  during graphite coating, the graphite layer on the carbon fiber unit can be made uniform by increasing the viscosity after coating by more than an order of magnitude.

As the  $\text{Al}_2\text{O}_3$  coating layer was chosen as the separator on the surface of the cylindrical negative-electrode, the mixing of particles of  $\text{Al}_2\text{O}_3$  in the slurry and graphite in the cylindrical negative-electrode must be avoided and the formation of cracks or micropores must be controlled during coating. Since an NMP-based slurry was used for bundling and twisting carbon fibers and coating graphite particles on the carbon fiber unit, it was assumed that an aqueous slurry would be preferred for coating the  $\text{Al}_2\text{O}_3$  separator. However, the NMP-based slurry of  $\text{Al}_2\text{O}_3$  with the PVDF binder must be used to form the separator to control the crack formation. As the NMP-based slurry to coat the  $\text{Al}_2\text{O}_3$  separator caused a short circuit, as previously assumed, an aqueous CMC slurry was coated on the cylindrical negative electrode before the  $\text{Al}_2\text{O}_3$ -separator coating. The application of a thin hydrophilic layer on the surface of the cylindrical negative electrode prevented the mixing of graphite and  $\text{Al}_2\text{O}_3$  particles during the  $\text{Al}_2\text{O}_3$ -separator coating process and dramatically improved short circuits after battery fabrication. It was confirmed that the thin hydrophilic layer between the cylindrical negative-electrode and the  $\text{Al}_2\text{O}_3$  separator does not interfere with lithium-ion transport and charge transfer reactions. As shown in Fig. S3 (ESI<sup>†</sup>), the viscosity of the slurry of  $\text{Al}_2\text{O}_3$  with PVDF dissolved in NMP for the  $\text{Al}_2\text{O}_3$  separator is almost constant in the shear rate region below  $10\text{ s}^{-1}$ . The slurry exhibits the characteristics of a Newtonian fluid in this region, meaning that the bumpy surface and micropores are likely to be generated in the  $\text{Al}_2\text{O}_3$  separator after coating if the



viscosity is adjusted to about 1000 mPa s during coating. Therefore, thin  $\text{Al}_2\text{O}_3$  layers were coated and dried twice to obtain a uniform separator without cracks and micropores.

Magnified images of the nozzle and shape of the electrode during the coating processes of the  $\text{Al}_2\text{O}_3$  separator and positive electrode are shown in Fig. 3(b). The positive electrode of  $\text{LiNi}_{1/3}\text{Co}_{1/3}\text{Mn}_{1/3}\text{O}_2$  was prepared by coating the slurry with PVDF dissolved in NMP on the  $\text{Al}_2\text{O}_3$  separator. Unlike the negative electrode, the slurry of the positive electrode can be uniformly coated without a thin hydrophilic layer by an aqueous CMC slurry on the  $\text{Al}_2\text{O}_3$  separator. As displayed in Fig. S3 (ESI<sup>†</sup>), the NMP-based slurry of the positive electrode belongs to the pseudoplastic fluid, which also exhibits shear-thinning behavior like the graphite negative electrode. A uniform and stable positive electrode can be prepared by a single coating of the slurry on the  $\text{Al}_2\text{O}_3$  separator, and the coaxial-fiber structure can be fabricated without short circuits between the positive and negative electrodes.

A 516 nm pulsed green laser with a galvanometer scanner was used to form the stepped structure of coaxial fibers. Processing rates of the positive electrode and separator, shown in Fig. 3(c), were measured separately by varying the energy density of the laser. A positive electrode, which has a laser-damage threshold close to  $0 \text{ J cm}^{-2}$ , can be processed even with a small energy density, whereas the separator must be processed with at least  $3 \text{ J cm}^{-2}$ . Positive electrodes can be

selectively removed at an energy density of  $2.6 \text{ J cm}^{-2}$  and with a separator at  $6.0 \text{ J cm}^{-2}$  to generate a current collection area on the carbon fiber unit, as shown in Fig. 3(c).

After the electrodes were cut into unit lengths, the positive electrode at both ends of the carbon fiber unit was selectively stripped using a laser to avoid short-circuiting between both electrodes and the separator was stripped to generate a current collection area. Coaxial-fiber electrodes were arranged and stacked in a row to form a 3D-electrode structure. The vertical/horizontal two-way pressing method, shown in Fig. 3(d), was developed to compress and densify the 3D-electrode. Current collecting tabs were connected to both electrodes, filled with electrolytes, and sealed with an aluminum laminated film to make CFBBs. The batteries are expected to enable charge-discharge operation without a copper current collector at the negative electrode owing to the high electrical conductivity of the carbon fiber unit and without applying binding pressure to the electrodes due to the bonding strength of the positive electrode composite.

### Electrochemical properties of a 15 mA h CFBB

Fig. 4(a) shows a single coaxial-fiber electrode of 113 mm length, in which cylindrical layers of the carbon fiber unit, separator, and positive electrode have a stepped structure. The carbon fiber unit has high electrical conductivity especially in charged states, as shown by the reversible and stable

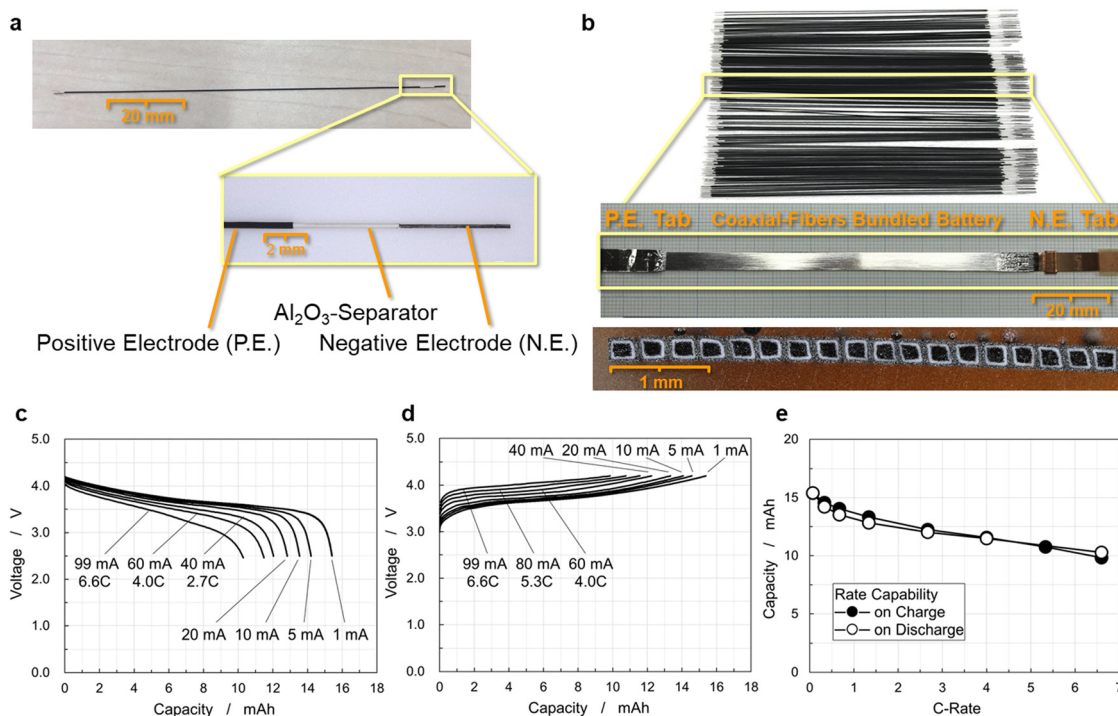


**Fig. 4** 15 mA h coaxial-fibers bundled battery (CFBB). (a) Photographs of a single coaxial-fiber electrode. (b) Photograph of a CFBB in which 18 single coaxial-fiber electrodes are arranged in a row. A thin aluminum foil of 8  $\mu\text{m}$  thickness as a current collector is wrapped around the positive electrode. Aluminum and copper tabs were connected to positive and negative electrode terminals, respectively. (c) Discharge curves of the battery during rate-capability tests upon discharge. The cells were charged at 1.0 mA to 4.2 V and held at that voltage for 2 h and then discharged at various currents from 1 to 99 mA at 20  $^{\circ}\text{C}$ . (d) Charge curves during rate-capability tests upon charge. The cells were discharged at 1 mA to 2.5 V and then charged at various currents from 1 to 99 mA at 20  $^{\circ}\text{C}$ . (e) Charge or discharge capacities as a function of the C-rates during the rate capability tests.



charge–discharge operation of the electrochemical cell of the carbon fibers as long as 210 mm displayed in Fig. S2 (ESI†). The length of carbon fibers was set at 113 mm and that of the coaxial-fiber electrode consisting of the carbon fiber unit, separator, and positive electrode was 98 mm to ensure sufficiently high rate capability. Cross-sectional images of the single coaxial-fiber electrode were observed at several locations using an optical microscope (Fig. S4, ESI†). The sizes with standard deviation  $\sigma$  of each component calculated by numerical analysis of the images are summarized in Table S2 (ESI†). The surface of the negative electrode was smoothed by coating graphite on the surface of the carbon fiber unit prepared by bundling and twisting 400 carbon fiber filaments, around which the  $\text{Al}_2\text{O}_3$  separator and then the positive electrode were coated coaxially. The size variation of each component of the coaxial-fiber electrode was small and the electrodes can be fabricated in a reproducible and stable manner. The average size of the coaxial-fiber electrode was 226  $\mu\text{m}$  diameter for the negative electrode, 17  $\mu\text{m}$  thickness for the  $\text{Al}_2\text{O}_3$  separator, and 46  $\mu\text{m}$  thickness for the positive electrode. As displayed in Fig. 4(b), many fiber electrodes were prepared, of which 18 were arranged in a row. The cross-sectional image displayed in Fig. 4(b) shows that the cross-section of the battery is rectangular, which indicates that the pressing method worked well to bundle and densify coaxial-fiber electrodes.

The appearance of the battery is also displayed in Fig. 4(b). The negative electrodes of carbon-fiber units without a current collector were connected to a copper tab at their ends; the positive electrode was sealed with an aluminum sheet as a current collector and was connected to an aluminum tab. The electrode body was sealed and filled with electrolytes. The battery was operated to examine the rate capability of the discharge and charge processes, as shown in Fig. 4(c) and (d), respectively. The battery exhibited a discharge capacity of 15.4 mA h under low-rate operation, in which a single coaxial-fiber electrode could store and deliver 0.86 mA h capacity.

The size, weight, and energy density of the 15 mA h CFBB are summarized in Table S3 (ESI†). The weight was calculated by converting the electrolyte weight in the electrode and separator from the electrode size and porosity. The dimensions of the 18 rectangular fibers as the electrode body were 0.349 mm height, 4.139 mm width, and 98 mm length, in which positive and negative electrodes faced each other *via* an  $\text{Al}_2\text{O}_3$  separator, and the weight of the cell including the electrolyte was 0.349 g. The energy density of the 15 mA h CFBB was calculated to be 403 W h  $\text{L}^{-1}$  by volume or 163 W h  $\text{kg}^{-1}$  by weight. Discharge capacity was 10.3 mA h at a 6.6C-rate, which corresponds to 67% capacity, and the battery exhibited comparable rate capability even upon charge, as displayed in Fig. 4(e). The 15 mA h CFBB with 18 fiber electrodes was successfully fabricated, which exhibited a high-rate capability for both charge and discharge.

### Improved safety of CFBBs

Safety mechanisms have been introduced in current LIBs, such as separator shutdown and container opening with disconnection using gas generation. In CFBBs, the separator was prepared by coating  $\text{Al}_2\text{O}_3$  with PVDF; therefore, the separator does not possess a shutdown mechanism. However, a reliable and safe battery that does not rely on a few isolated technologies must be fabricated. A fundamental solution to the safety issue arising from the characteristic fiber-bundled structure is required for CFBBs. Electrochemical-thermal coupled simulations were performed to predict safety in the event of an internal short circuit. Fig. 5(a) and (b) display the battery models of sandwich-type and fiber-bundled structures, respectively. The short-circuit point in the cell was cylindrical with a diameter of 10 mm and a thickness of 1 mm. The simulated temperature distributions inside the cells are also displayed. The sandwich-type structure exhibited substantial heat generation and dispersion in the battery. In a fiber-bundled structure, heat generation is limited because the current flow to each of

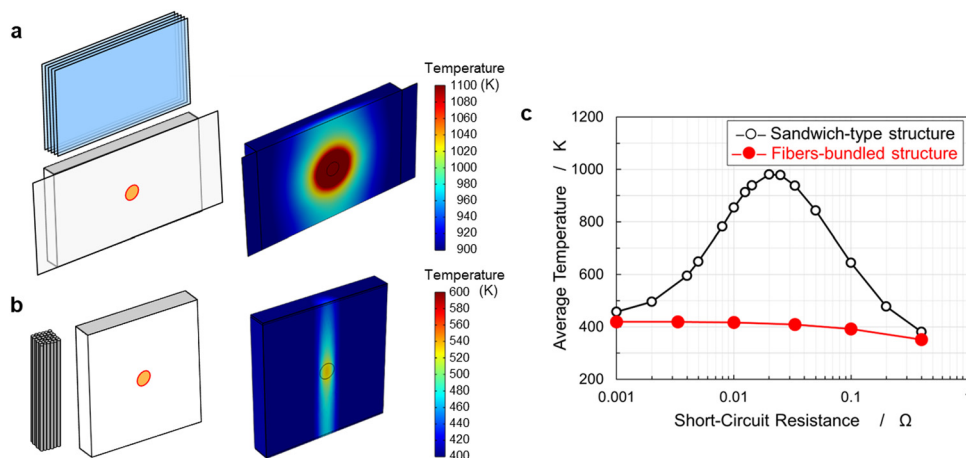


Fig. 5 Simulated temperature distribution inside the batteries and the maximum average temperature. (a) Battery model and simulated temperature distribution of the sandwich-type structure at the maximum temperature. (b) Battery model and simulated temperature distribution of the fiber-bundled structure at the maximum temperature. (c) Maximum average temperature of the batteries with sandwich-type and fiber-bundled structures as a function of short-circuit resistances.





the coaxial fiber electrodes is small. Fig. S5 (ESI<sup>†</sup>) shows variation of the temperature distribution in the fiber-bundled structure over time. Heat does not spread across the fiber bundles, while heat release through the carbon fibers prevents further heat generation in the battery.<sup>47</sup> Fig. 5(c) shows the maximum average temperature of the electrode. The sandwich-type structure exhibited a considerable temperature rise when the short-circuit resistance was equal to the internal resistance of the battery; however, the fiber-bundled structure did not show noticeable heat generation regardless of the short-circuit conditions. Therefore, CFBBs are expected to be safe as they suppress current flow and prevent heat spread.

### Rate capability and safety of a 225 mA h CFBB consisting of 288 fiber electrodes

CFBBs consisting of 288 fiber electrodes were fabricated to examine the rate capability, cycling life, and safety. Cross-sectional images obtained using an X-ray computed tomography (CT) scan are displayed in Fig. 6(a), which shows that each small square is a single coaxial-fiber battery and white lines indicate the positive electrode. The vertical/horizontal two-way pressing method densified and bundled the fiber electrodes uniformly. Fig. 6(b) shows the rate-capability of the CFBB consisting of 288 fiber electrodes. The battery was successfully fabricated to have a discharge capacity of 225 mA h. The energy density of the 225 mA h CFBB was calculated to be 382 W h L<sup>-1</sup> by volume or 151 W h kg<sup>-1</sup> by weight. As displayed in Fig. 6(b), the battery exhibited a discharge capacity of 180 mA h at a 7.6 C-rate, which corresponds to 81% of 225 mA h. To examine the basic performance of CFBBs, a sandwich-type multi-sheet battery of equivalent size and shape to a CFBB was fabricated for comparison, in which an LiNi<sub>1/3</sub>Co<sub>1/3</sub>Mn<sub>1/3</sub>O<sub>2</sub> positive electrode

of 10 and 100 mm width and length, respectively, and a graphite negative electrode of 11 and 100 mm were stacked and separated using a polyethylene separator. Fig. S6(a) (ESI<sup>†</sup>) displays the sandwich-type structure and the sealed battery, in which 19 sheets of the positive electrode and 20 sheets of the negative one were stacked. The battery was operated by pressing the stacked electrodes from outside the pouch, and the rate capability is shown in Fig. S6(b) (ESI<sup>†</sup>). The discharge capacity of the battery is shown in Fig. S6(c) (ESI<sup>†</sup>). The discharge capacity was 1012 mA h at a low rate and then decreased rapidly to 205 mA h at a 5.9C-rate and 113 mA h at a 7.9C-rate. The CFBBs were found to exhibit superior rate capability to a sandwich-type multi-sheet battery. Energy densities and rate capability of the commercial lithium-ion batteries are summarized in Table S4 (ESI<sup>†</sup>). The maximum currents of the commercial lithium-ion battery of LP603449 with energy density equivalent to the CFBBs are shown in the datasheet to be 1C-rate upon charge and 2C-rate upon discharge. A cylindrical lithium-ion battery of INR18650-MJ1 with a higher energy density than those of the CFBBs is shown in the datasheet to have maximum currents of 1C-rate upon charge and 3C-rate upon discharge.<sup>48</sup> Scheller *et al.* examined the fast-charging capability of several cylindrical lithium-ion batteries and their results on capacity, energy densities, and capacity retention on 4C-rate charge in comparison to low-rate charge are listed in Table S4 (ESI<sup>†</sup>).<sup>49</sup> They reported that the capacity retention values of 4C-rate charging are 21–29% compared to low-rate charging. As shown in Fig. 4(c)–(e) and 6(b), the CFBBs exhibited about 80% of capacity retention at a 4C-rate upon both charge and discharge. These results indicate that CFBBs have rapid charge and discharge capabilities.

The nail penetration test of CFBBs was performed and the experimental setup is displayed in Fig. S7 (ESI<sup>†</sup>). Thermocouples

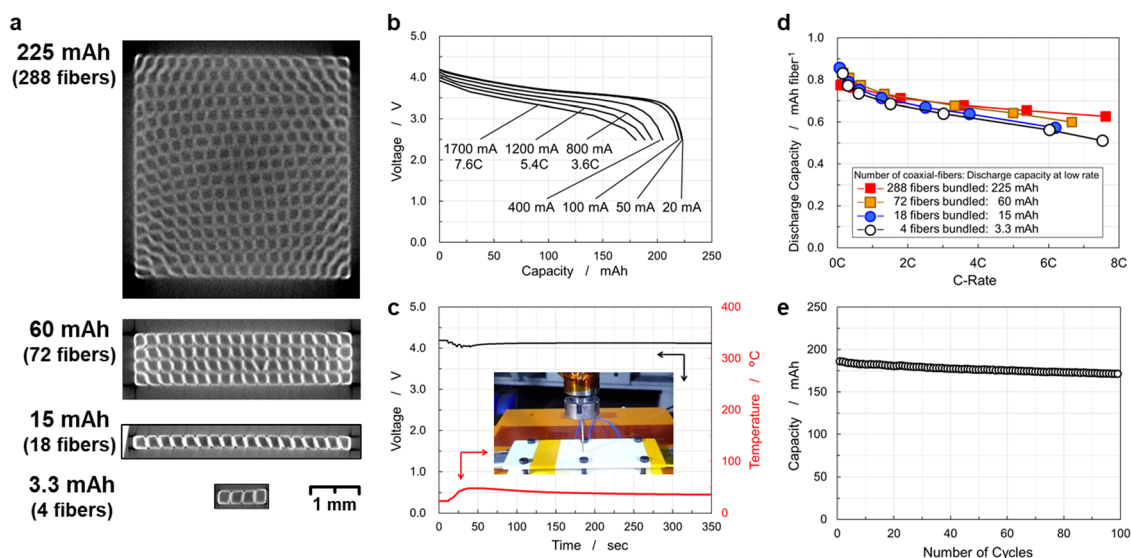


**Fig. 6** 3–225 mA h coaxial-fibers bundled batteries (CFBBs). (a) Cross-sectional images of the CFBBs using X-ray CT scan. (b) Discharge curves of a 225 mA h battery during the rate-capability test upon discharge. The cell was charged at 60 mA and held at that voltage for 2 h and then discharged at various currents from 50 to 1700 mA at 20 °C. (c) The change in the voltage and temperature of the 225 mA h CFBB during the nail penetration test, and a photograph of the experimental setup. (d) Discharge capacities of the CFBBs normalized by the values per single coaxial-fiber electrode during the rate-capability test. (e) Capacity retention of the 225 mA h CFBB operated in a voltage window of 3.0–4.1 V at a 0.7C-rate at 20 °C.





were placed 7 mm from the nail at two locations on the battery. A 1012 mA h sandwich-type battery in a fully charged state of 4.2 V was also tested and the setup is displayed in Fig. S6(a) (ESI†). The battery was held in place by a plastic plate and a nail was inserted at a speed of  $0.1 \text{ mm s}^{-1}$  to a depth of 4 mm into the 7 mm thickness of the stacked electrodes. The temperature change was measured during the nailing process. Fig. S6(d) (ESI†) shows the changes in the voltage and temperature of the sandwich-type multi-sheet battery during the test. The voltage suddenly dropped at 30 s and after a few seconds, a rapid temperature rise occurred to a maximum temperature of  $605^\circ\text{C}$  and the battery ignited. For the nail penetration test of the CFBB, under conditions equivalent to those of the sandwich-type battery, the capacity of the CFBB of 225 mA h was brought to the same level as that of the sandwich-type battery for comparison. A lithium-ion battery with a capacity of 1100 mA h at 3.7 V available on the market was connected in parallel in a charged state of 4.2 V to the CFBB for the nail penetration test after the protection circuit module (PCM) attached to the commercial lithium-ion battery was removed from the battery as the PCM has high resistance. When connecting the batteries in parallel, thick and low-resistance cables of about  $6 \text{ m}\Omega$  in short sizes were used to facilitate current supply to the short-circuit point. The nail penetration test of a 1300 mA h CFBB was conducted by connecting the 1100 mA h commercial battery in parallel to a 225 mA h CFBB using the low-resistance cable. The CFBB was held in place by a plastic plate and the test was performed under the same conditions as the sandwich-type battery on the 4.8 mm thick bundled electrodes. Fig. 6(c) shows the voltage and temperature of the batteries during the test. As the nail penetrates, current flows to the short circuit from the electrodes in the CFBB as well as the commercial battery connected in parallel. The voltage drop associated with nail penetration was limited to 4.02 V, and the maximum temperature of the CFBB measured by the thermocouples was as low as  $48^\circ\text{C}$ . Note that the nail penetration test of the 1100 mA h commercial battery, which was used in parallel connection, resulted in a rapid temperature rise and ignition.

When a nail is inserted into the sandwich-type multi-sheet battery, a large current flows from the entire electrode through the aluminum and copper current collectors, which have the lowest resistance in the battery, to the short-circuit point, leading to the thermal runaway of the battery. As the CFBBs have the characteristic fiber-bundled structure, current flows only through the short-circuited electrodes. Inserting a nail with a width of 1 mm to a depth of 4 mm in a CFBB will short-circuit about 64 of the total 288 fiber-bundled electrodes. Coaxial-fiber electrodes involved in the short circuits are limited to 22% of the total number of electrodes. In the event of the short circuit of the coaxial-fiber bundled electrode, a small current flows through the components with higher resistance of 7  $\mu\text{m}$ -thick thin aluminum sheets and the carbon fibers. Heat generation was suppressed by these two factors and heat release proceeded through the carbon fibers. As a result, the temperature rise was suppressed in the CFBB. It could be demonstrated that the safety mechanism of CFBBs works well

to suppress the temperature rise, even if the commercial battery is used as a capacity buffer.

### Battery performance of CFBBs and demonstration of the size/shape flexibility

In sandwich-type structures, negative electrodes are generally designed to be a few millimeters larger in length and width than the positive ones to prevent the formation of dendritic lithium on the negative electrode. Large batteries can disregard the effect of the size difference between both electrodes. However, the loss of energy density and degradation of capacity may become apparent in small-sized batteries due to unpaired areas in the negative electrodes and the resulting lithium-ion leakage into them. CFBBs were fabricated by bundling coaxial-fiber electrodes; therefore, the size and capacity of CFBBs can be controlled by changing the number of coaxial-fiber electrodes. CFBBs are expected to be scalable, meaning that equivalent battery performance can be expected irrespective of capacity, including in small-sized batteries. CFBBs consisting of 72, 18, and 4 fiber electrodes were fabricated to compare with the 288-fiber electrode CFBBs to examine the flexibility in size and shape. Cross-sectional images obtained by X-ray CT scan of the CFBB consisting of 288, 72, 18, and 4 fiber electrodes are displayed in Fig. 6(a). Irrespective of the number of electrodes, the vertical/horizontal two-way pressing method worked well in densifying and bundling the fiber electrodes. The CFBBs with 72, 18, and 4 fiber electrodes were successfully fabricated and achieved capacities of 60, 15, and 3.3 mA h, respectively. The energy densities of the CFBBs are summarized in Table S3 (ESI†). The energy densities were in the range of  $382\text{--}410 \text{ W h L}^{-1}$  by volume or  $151\text{--}163 \text{ W h kg}^{-1}$  by weight. Fig. S8 (ESI†) shows the rate-capabilities of 60 and 3.3 mA h CFBBs and Fig. 6(d) shows the discharge capacities of the CFBBs during the rate-capability test. The capacities were normalized by the values per single coaxial-fiber electrode. Irrespective of the size of the CFBBs, the batteries exhibited identical rate-capability below 4C. The 3.3 mA h CFBB with 4 fiber electrodes exhibited 51% capacity retention at a 7.5C rate and the 60 and 225 mA h-class CFBBs showed higher capacity retention above 4C. High electric-current flows through the CFBB during battery operation at high rates.

The temperature increase of the carbon fiber owing to high electric-current flow is estimated to reveal the difference in the rate capability at high rates. Although the volume resistivity of the carbon fiber measured in this paper was  $3.4 \times 10^{-3} \Omega \text{ cm}$ , the resistance between both ends of the carbon fiber unit measured at 1 kHz decreased in the charged states, suggesting a decrease in volume resistivity with charging. Since the resistance at 1 kHz decreased to 16% of the initial value in the charged state of SOC 50%, the volume resistivity in the charged state was assumed to be  $5.44 \times 10^{-4} \Omega \text{ cm}$ . The resistance of the carbon fibers in each CFBB was calculated from the volume resistivity in the charged state and the size and weight of the carbon fibers. The Joule heat generated in the carbon fiber was calculated from the electric current and discharge time during high-rate discharge, and the temperature increase owing to



high electric-current flow was estimated by assuming the specific heat capacity of  $0.71 \text{ J g}^{-1} \text{ K}^{-1}$  equivalent to that of graphite.<sup>50</sup> The results are summarized in Table S5 (ESI†). The temperature increases were estimated to be 195–229 °C from room temperature irrespective of the number of fiber electrodes in the CFBBs. The temperature increase may be a factor responsible for the increase in discharge capacity at high rates owing to the increase in the number of fiber electrodes in CFBBs. As shown in Fig. 6(d), the 225 mA h CFBB exhibited the highest rate capability among the CFBBs. This means that even with the increase in the number of fiber electrodes, the increase in the internal temperature of CFBBs is limited in comparison to the remarkable temperature increase shown in Table S5 (ESI†). This may be attributed to the rapid heat release of carbon fibers inside CFBBs. To verify the relationship between temperature increase owing to the Joule heat and the heat release through the carbon fibers, the high energy-density CFBB with 36 fiber electrodes was fabricated with the increased capacity of a single coaxial-fiber electrode. The size, weight, and energy density of the CFBB are also listed in Table S3 (ESI†). The rate capability of the CFBB is displayed in Fig. S9(a) (ESI†). The discharge capacities of the CFBB normalized by the values per single coaxial-fiber electrode during the rate-capability test are shown in Fig. S9(b) (ESI†). The discharge capacity of a single coaxial-fiber electrode increased to 0.973 mA h, which indicates that CFBBs can be fabricated with high capacity and high energy density. The calculated temperature increase of the high energy-density CFBB is shown in Table S5 (ESI†). Although the temperature increase of the high energy-density CFBB during high-rate discharge was estimated to be 305 °C, which is almost 100 °C higher than the other CFBBs fabricated, the high energy-density CFBB exhibited capacity retention comparable to those

of other CFBBs during the rate capability test. The results for the high energy-density CFBB also suggest the rapid heat release of carbon fibers inside the CFBBs. Irrespective of the number of fiber electrodes, CFBBs exhibited excellent rate capability, with even the small-sized CFBB consisting of 4 fiber electrodes showing sufficient capacity retention at high rates. The CFBBs were operated without any external constraining pressure on the electrodes. In contrast, a sandwich-type structure requires the application of constraining pressure from outside the battery. This means that CFBBs can exhibit comparable rate capabilities irrespective of capacity without any constraining pressure and the structural feature of CFBBs provides the flexibility in size and shape.

To examine the durability, a charge–discharge cycling test of a 225 mA h battery was performed at 4.1–3.0 V at a 0.7C-rate at 20 °C, as shown in Fig. 6(e). The initial discharge capacity was 186 mA h, which lowered to 171 mA h after 100 cycles, corresponding to 92% capacity retention. The battery exhibited stable charge–discharge behavior over 100 cycles without significant degradation of the coaxial-fiber electrodes. To demonstrate the performance of the CFBBs, four batteries, each consisting of 288 fiber electrodes, were fabricated and integrated into a drone, as displayed in Fig. 7(a) and (b) (see also Supplementary Video 1, ESI†). The drone rose 1–1.5 m in height and flew steadily. The batteries removed from the drone can be recharged and reassembled to repeat drone flights multiple times. Batteries with several hundred electrodes were demonstrated to be suitable for drone flight. In addition to ensuring the battery performance of the CFBBs, the mechanical properties of the CFBBs consisting of 288 fiber electrodes were examined by conducting a flexure test to apply them as the frameworks of the devices themselves. Fig. 7(c) shows the

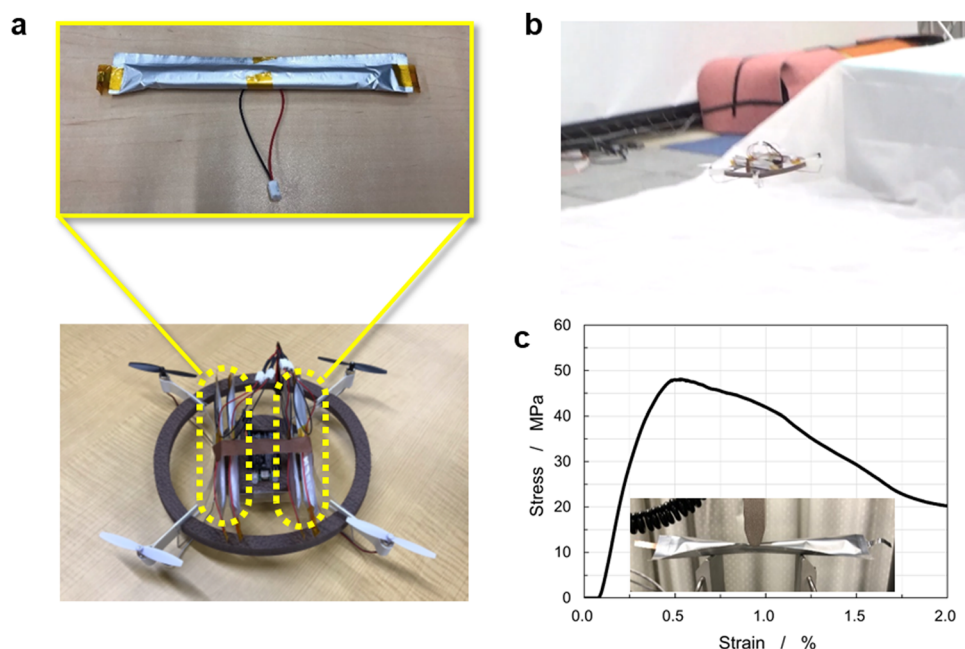


Fig. 7 (a) Photograph of a drone with four 225 mA h CFBBs. A pouch cell with wiring of a 225 mA h CFBB is also displayed in the inset. (b) Photograph of the test flight. (c) Stress–strain curve of the 225 mA h CFBB and the experimental setup.



stress-strain curve of the CFBB during the test and the experimental setup is displayed in the inset. The flexural modulus of the CFBB consisting of 288 fiber electrodes was calculated to be 19.3 GPa from the slope in the elastic region, which is equivalent to that of a glass-fiber-reinforced plastic. CFBBs were demonstrated to have sufficiently high strength to be applied as the frameworks of drones and wearable devices such as smart glasses. Fig. S10 (ESI†) shows the capacity retention of a 3.3 mA h CFBB in a voltage window of 4.1–3.0 V at a 0.7C-rate at 20 °C for 100 cycles. The discharge capacity after 100 cycles is 2.11 mA h, in comparison to the initial capacity of 2.37 mA h, which corresponds to 90% capacity retention.

In sandwich-type structures, battery performance deteriorates easily owing to the adverse effect of the unpaired area of the negative electrode as the electrode becomes smaller. CFBBs have an axial symmetry in the electrode structure and thus exhibit excellent capacity retention even in small batteries. CFBBs exhibited sufficient flexibility in size and shape necessary to design any form of battery package. New applications emerging from future technological innovations, such as smart devices represented by drones, robotics, smart glasses, and smart cards with displays, require batteries to be small and slender in shape in addition to being strong enough to be applied as the frameworks of the devices.

## Conclusion

This study proposed CFBBs, which comprise a single central carbon fiber unit (negative electrode), an inner shell (separator), and an outer shell (positive electrode), to achieve high energy density and high-rate capability during discharging and charging and safety in the event of an internal short circuit. The carbon fiber serves as a current collector without requiring copper foil, contributing to increased energy density and eliminating the resource scarcity risk of copper. The coaxial fiber structure increases the electrode-facing area and shortens the ionic conduction pathway in the electrodes, increasing the charge-discharge capability. The highly reproducible electrode fabrication of the coaxial fiber structure to prevent short circuits was achieved by adjusting the viscosity of slurries and multilayer coatings.

CFBBs can operate at a high rate without constraining pressure due to the vertical/horizontal two-way pressing of the bundle. CFBBs exhibited superior rate capability compared to a sandwich-type multi-sheet battery and were flexible in terms of size and shape, which can be controlled by changing the number of coaxial-fiber electrodes. Electrochemical-thermal coupled simulations predicted that CFBBs are safe as they suppress current flow and prevent heat spread in the event of an internal short circuit. In addition, the nail penetration test demonstrated that the safety mechanism works well within CFBBs to suppress the temperature rise. CFBBs have strength equivalent to glass-fiber-reinforced plastics and structural features that allow for compact size and slender shape, making them suitable for application as the frameworks of drones,

robotics, and wearable devices, such as smart glasses, and as their power sources. The characteristic features of CFBBs meet the future requirements of emerging technologies.

## Experimental section

### Materials

Pitch-based carbon fibers (Nippon Graphite Fiber Corporation, Japan), in which 400 carbon fibers of approximately 7 µm in diameter were bundled as a yarn, were used as a negative electrode in CFBBs. P(VDF/HFP) (Kureha, Japan) dissolved in NMP was used to fix the circular shape of the carbon fiber unit. The electrode slurry of 97 wt% graphite TIMREX SFG6 (TIMCAL, Ltd, Switzerland) and 3 wt% PVDF (Kureha, Japan) dissolved in NMP was coated on carbon fibers to be the cylindrical negative electrode and a small amount of aqueous CMC slurry was coated on the negative electrode to improve short-circuits between the positive and negative electrodes after battery fabrication. The white slurry for the separator coating was prepared by mixing powdered Al<sub>2</sub>O<sub>3</sub> (D50: 0.88 µm, Sumitomo Chemical Co., Ltd, Japan) with PVDF (Kureha, Japan) dissolved in NMP at a 90:10 weight ratio. LiNi<sub>1/3</sub>Co<sub>1/3</sub>Mn<sub>1/3</sub>O<sub>2</sub> (Toda Kogyo Corporation, Japan), acetylene black (Denka Co. Ltd, Japan), and PVDF dissolved in NMP were mixed in an 88:6:6 weight ratio to prepare a black viscous slurry for the positive electrode. The electrolyte used to fabricate electrochemical cells of CFBBs was 1 M LiPF<sub>6</sub> dissolved in ethylene carbonate (EC), dimethyl carbonate (DMC), and ethyl methyl carbonate (EMC) in a 3:4:3 volume ratio solution (Kishida Chemical Co. Ltd, Japan).

### Estimation of energy densities and electrode areas

The energy density and electrode area of a single coaxial-fiber battery were estimated and compared with those of a conventional sandwich-type multi-sheet battery as a function of the thickness of the negative electrode by assuming the structural parameters listed in Table S1 (ESI†). The thickness of the negative electrode in the CFBB corresponds to the radius of the carbon fiber unit. In the single coaxial-fiber battery, a carbon fiber unit exhibited 330 mA h g<sup>-1</sup> discharge capacity and the cylindrical negative electrode was assumed to have an electrode density of 1.86 g cm<sup>-3</sup> in the total volume. The negative electrode did not include a copper current collector because the carbon fiber served as a current collector. The separator used to isolate the positive and negative electrodes was Al<sub>2</sub>O<sub>3</sub> particles with PVDF at 90:10 wt% and a thickness of 15 µm. The positive electrode consisted of 88 wt% LiNi<sub>1/3</sub>Co<sub>1/3</sub>Mn<sub>1/3</sub>O<sub>2</sub>, showing a discharge capacity of 150 mA h g<sup>-1</sup>, 6 wt% acetylene black, and 6 wt% PVDF binder with an electrode density of 2.8 g cm<sup>-3</sup>. An aluminum sheet with a thickness of 7 µm was inserted into every two rows of plate-shaped bundled electrodes to serve as the current collector of the positive electrode. The volume of the aluminum current collector was multiplied by 0.5 because the collector was attached to one side



of the cylindrical shape and further multiplied by 0.25 because one current collector was used per four coaxial-fiber electrodes.

In the conventional sandwich-type battery, the negative electrode consisted of 98 wt% graphite, which exhibited a discharge capacity of  $330 \text{ mA h g}^{-1}$ , and 2 wt% binder with an electrode density of  $1.6 \text{ g cm}^{-3}$  with a  $10 \text{ }\mu\text{m}$  thick copper sheet as a current collector. A porous polyethylene film of  $15 \text{ }\mu\text{m}$  thickness was used as the separator. The positive electrode was assumed to have a composition of 88 wt%  $\text{LiNi}_{1/3}\text{Co}_{1/3}\text{Mn}_{1/3}\text{O}_2$ , 6 wt% acetylene black, and 6 wt% PVDF binder with an electrode density of  $2.8 \text{ g cm}^{-3}$ . The current collector was a  $15 \text{ }\mu\text{m}$ -thick aluminum sheet. The capacity in  $\text{mA h}$  of the negative electrode was designed to be 1.1 times larger than that of the positive electrode and the charge-discharge operations of the batteries were limited by the voltage and capacity of the positive electrode.

### Preparation of carbon fiber units as a negative-electrode and pouch-cell fabrication

Four hundred carbon fiber filaments were bundled and twisted: the filaments were drawn from the rotating top spool and passed through the nozzle where they were coated with P(VDF/HFP) dissolved in NMP, as shown in Fig. 3(a). The cylindrical carbon fibers were dried by passing them through heaters and wound onto an empty spool at the bottom. The carbon fibers were cut into unit lengths and P(VDF/HFP) was stripped from the surface in  $5 \text{ mm}$  length of the carbon fibers at both ends for terminal connections. A pouch-type electrochemical cell was used to examine the electrochemical behavior and changes in the physical properties of the carbon fiber unit. The carbon fiber unit was covered with a polyethylene separator and coated with lithium metal sheets from both the front and back sides. Copper tabs were attached to both ends of the carbon fiber unit as a working electrode and nickel tabs were attached to lithium metal sheets as a counter or reference electrode. The change in the electrical resistance of the carbon fiber unit was examined by fabricating a cell from a single  $210 \text{ mm}$  long carbon fiber unit coated with a  $200 \text{ mm}$  long lithium-metal sheet in an argon-filled glove box. A  $210 \text{ mm}$  long carbon fiber unit was weighed before cell fabrication, and the mass equivalent to that of a  $200 \text{ mm}$  long fiber was used to calculate the capacity in  $\text{mA h g}^{-1}$ . The cell was charged to  $0.005 \text{ V}$ , which corresponds to the reduction of the working electrode, in the constant-current constant-voltage (CCCV) mode at a C/10-rate based on a capacity of  $300 \text{ mA h g}^{-1}$  and held at that voltage for  $2 \text{ h}$  at  $20 \text{ }^\circ\text{C}$ . The cell was then discharged, or the working electrode was oxidized, to  $1.5 \text{ V}$  in the CCCV mode at a C/10-rate and held for  $2 \text{ h}$ . The charged state at  $0.005 \text{ V}$  was defined as a SOC 100%. After the charge-discharge operation was performed for three cycles, the cell was charged to  $0.005 \text{ V}$  in a CCCV mode corresponding to SOC 100%, in which lithium was intercalated into the carbon fiber unit. The electrical resistance between both sides of the carbon fiber unit at SOC 100% was measured at  $1 \text{ kHz}$  using a battery tester (Battery HiTester 3561, Hioki, Japan). After measuring the electrical resistance at SOC 100%, the cell was discharged, or the working electrode was oxidized, at SOC 75% and the electrical resistance

was measured at  $1 \text{ kHz}$ . Similarly, the working electrode was then oxidized at SOC 50, 25, and 0% and the corresponding electrical resistances were measured. The electrochemical cell of a single  $130 \text{ mm}$  long carbon fiber unit coated with a  $120 \text{ mm}$  long lithium-metal sheet was also fabricated, and the electrochemical behavior was examined in a voltage window of  $0.005\text{--}1.5 \text{ V}$  in CCCV mode at a C/10-rate at  $20 \text{ }^\circ\text{C}$ .

### Morphology characterization

The surface and cross-section of the carbon fiber units were observed using scanning electron microscopy (SEM, S-4300, Hitachi, Ltd, Japan). Cross-sectional images of the single coaxial-fiber electrode or the CFBBs were obtained using a digital microscope (VHX-7000, Keyence, Japan). Cross-sectional images of the CFBBs were also obtained using a 3D X-ray microscopic CT scanner (TDM1000H-II, Yamato Scientific Co., Ltd, Japan).

### Preparation of CFBBs

After the carbon fiber was coated with P(VDF/HFP) and twisted into a cylindrical shape, the bottom spool wound with the coated carbon fiber was replaced with the upper spool, and another empty spool was installed at the bottom. The electrode or separator slurry was coated over the surface of the coaxially coated fiber electrode and dried by passing it through a heater and the bottom spool was replaced by the top spool for multi-layer coatings. The coaxially coated fiber electrodes were cut into unit lengths of  $113 \text{ mm}$  and the positive electrodes at both ends of the carbon fiber unit of nine and four millimeters were removed using a laser to avoid short-circuiting between the positive and negative electrodes. Then,  $5 \text{ mm}$  of one side of the separator was removed to generate a current collection area on the carbon fiber unit. A pulsed green laser (Pulsed Green Nanosecond Fiber Laser, GLPN-500-1-50-M, IPG Photonics Corp.) with a wavelength of  $516 \text{ nm}$ , a pulse duration of  $1 \text{ ns}$ , and a repetition frequency of  $1 \text{ MHz}$  and a galvanometer scanner (MIRAMOTION, YD-300-532-P, YE Data Inc.) to scan the laser were used to selectively remove the positive electrode and separator at energy densities of  $2.6$  and  $6.0 \text{ J cm}^{-2}$ , respectively, from the surface of the carbon fiber unit. The longitudinal processing accuracy of the laser was  $\pm 0.01 \text{ mm}$ . Coaxial-fiber electrodes were arranged in a row to form a flat plate, and an aluminum sheet ( $7 \text{ }\mu\text{m}$  thickness) was placed on the single-plated electrode. The plated electrode and aluminum sheet were pressed together using the vertical/horizontal two-way pressing method with  $30 \text{ kN}$  applied independently from the two directions orthogonal to the central axis of the electrode body at  $100 \text{ }^\circ\text{C}$ . A coaxial fiber-bundled structure with more than 18 electrodes was fabricated by stacking the plated electrodes with a pressed aluminum sheet. Copper tabs were attached to the carbon fiber units with a crimp sleeve. The bundled electrodes were packed in an aluminum-laminated film and then filled with electrolytes to make CFBBs.

### Preparation of sandwich-type multi-sheet batteries

A black viscous slurry of the positive electrode mix consisting of 88 wt%  $\text{LiNi}_{1/3}\text{Co}_{1/3}\text{Mn}_{1/3}\text{O}_2$ , 6 wt% carbon black, and 6 wt%





PVDF binder dissolved in NMP was painted on both sides of aluminum foil and dried under vacuum conditions at 120 °C for 8 h. The painted sheets were pressed to increase electrode density and cut to form the positive electrodes. Graphite negative electrodes were prepared in the same way as the positive electrode and consisted of 98 wt% graphite, 1 wt% CMC, and 1 wt% SBR coated on copper foil. The weight of one side of  $\text{LiNi}_{1/3}\text{Co}_{1/3}\text{Mn}_{1/3}\text{O}_2$  coated on the aluminum foil was about 20  $\text{mg cm}^{-2}$  and that of graphite on copper foil was 12  $\text{mg cm}^{-2}$ .

Sandwich-type multi-sheet batteries of equivalent size and shape to the CFBBs were fabricated, in which 19 sheets of the  $\text{LiNi}_{1/3}\text{Co}_{1/3}\text{Mn}_{1/3}\text{O}_2$  positive electrode of 10 mm width and 100 mm length and 20 sheets of the graphite negative electrode of 11 and 100 mm were stacked with a polyethylene separator between them. The electrodes were packed in an aluminum-laminated film and then filled with electrolytes. The battery was operated by pressing the stacked electrodes from outside the pouch.

### Rate-capability and charge-discharge cycling tests of CFBBs

A low-rate charge-discharge operation was performed once to activate the CFBBs and a rate capability test upon discharge was conducted at 20 °C. The CFBBs were charged at an approximately C/10-rate to 4.2 V and held at that voltage for 2 h in the CCCV mode and then discharged to 2.5 V at various currents between C/30- and 7.6 C-rates in the constant-current (CC) mode. The C-rates were determined based on the discharge capacity at a low-rate charge-discharge operation. For the 15 mA h CFBB, a rate-capability test upon charge was also performed, in which the CFBB was charged to 4.2 V at various currents from the C/30- to 6.6C-rate in the CC mode and discharged to 2.5 V at the C/30-rate. The currents and C-rates during the rate capability tests of the CFBBs are summarized in Table S6 (ESI†). Charge-discharge cycle testing for 3 and 225 mA h CFBBs was performed in a voltage window of 3.0–4.1 V at a 0.7C-rate for 100 cycles at 20 °C.

### Electrochemical-thermal coupled simulations

An LIB short-circuit is simulated as two phenomena: discharge and thermal diffusion.<sup>51–56</sup> LIB discharge can be described by the following models and equations.<sup>51</sup> The electric current was calculated using Ohm's law:

$$I = \frac{V}{R} \quad (1)$$

where  $I$  is the electric current,  $V$  is the voltage, and  $R$  is the resistance, which includes LIB internal resistance, current collector (copper and aluminum) resistance, and contamination resistance (which causes a short-circuit, such as Li deposition on a piece of metal). The voltage was determined by the lithium concentration in the carbon and nickel-based layered positive electrodes. A fully charged voltage of 4.2 V was used as an initial condition. The current collectors of a coaxial-fiber battery cause longer paths to the short-circuit point or area to offer resistance much larger than that of conventional current

collectors. Contamination resistance depends on short-circuit conditions;<sup>52,56</sup> hence, it has been parametrically studied.

Based on the defined electric current, the electrochemical reaction at the electrode interface can be calculated using the following Butler-Volmer equation:

$$I = I_0 \left\{ \exp \left[ \frac{0.5F\eta}{RT} \right] - \exp \left[ -\frac{0.5F\eta}{RT} \right] \right\} \quad (2)$$

where  $I_0$  is the exchange current,  $F$  is Faraday's constant,  $\eta$  is the overpotential of the intercalation reaction,  $R$  is the universal gas constant, and  $T$  is the electrode temperature. Inside porous electrodes, Newman's model (pseudo two-dimensional (P2D) model)<sup>51</sup> describes electron and lithium transfer. As a result, the lithium distribution between the electrodes changes the voltage. When the voltage reached 2.4 V, this simulation was terminated.

Thermal diffusion of electrodes obeys Fick's law:

$$\rho C_p \frac{dT}{dt} = k \nabla T + Q_h + Q_j \quad (3)$$

where  $\rho$  is the density,  $C_p$  is the heat capacity at constant pressure,  $t$  is the time,  $k$  is the thermal conductivity,  $Q_h$  is the enthalpy change inside the electrodes, and  $Q_j$  is the Joule heat at the internal short-circuit point or area. Since carbon fiber has high conductivity, it is expected to affect the thermal distribution. The temperature rise may enhance the chemical reaction and lithium diffusion,<sup>53–55</sup> enabling the interaction of discharge and thermal diffusion.

COMSOL Multiphysics<sup>®</sup> (version 6.0, the Battery Design module and Heat Transfer module) was used to perform this simulation, and the electrode temperature was obtained based on the contamination resistance.

### Nail penetration test

K-type thermocouples were placed 7 mm from the nail at two locations on the battery. The battery was held in place by a plastic plate and a nail with a width of 1 mm was inserted at a speed of 0.1  $\text{mm s}^{-1}$  to a depth of 4 mm into the 7 mm thickness of the stacked electrodes. The temperature change was measured during the nailing process and subsequently with the nail inserted. To perform the nail penetration test under equivalent conditions on a 1000 mA h sandwich-type multi-sheet battery and a 225 mA h CFBB, a commercial lithium-ion battery with a capacity of 1100 mA h at 3.7 V (LP603449-PCM, EEMB Co., Ltd, China) was connected in parallel to the CFBB in a charged state of 4.2 V after the protection circuit module (PCM) attached to the commercial lithium-ion battery was removed from the battery since the PCM has a high resistance. When connecting the batteries in parallel, thick and low-resistance cables of about 6 mΩ in short sizes were used to facilitate current supply to the shot circuit point.

### Flexure test of a 225 mA h CFBB

A three-point bending test was performed using an Instron 4302 universal testing machine at a constant crosshead speed



of 1 mm min<sup>-1</sup> with a support span of 70 mm to examine the flexural stress-strain response of a 225 mA h CFBB.

## Author contributions

Y. Makimura: conceptualization, data curation, formal analysis, investigation, methodology, visualization, writing – original draft, writing – reviewing and editing; C. Okuda: conceptualization, data curation, formal analysis, investigation, methodology, visualization, supervision, writing – original draft, writing – reviewing and editing; T. Munekata: data curation, formal analysis, investigation, methodology, software, visualization, writing – original draft; A. Tsukigase: data curation, formal analysis, investigation, writing – original draft; H. Oka: data curation, formal analysis, investigation, methodology, writing – original draft, writing – reviewing and editing; T. Saeki: data curation, formal analysis, visualization; R. Morimoto: data curation, formal analysis, visualization; M. Sasaki: data curation, visualization; H. Nakano: data curation, formal analysis; Y. Itou: data curation, formal analysis, visualization; M. Mizutani: data curation; and T. Sasaki: conceptualization, funding acquisition, investigation, methodology, project administration, resources, supervision, writing – original draft, writing – reviewing and editing. All authors read the manuscript and contributed to the discussion of the results.

## Conflicts of interest

The authors declare no competing financial interest.

## Acknowledgements

We are grateful to Nippon Graphite Fiber Corporation for providing the carbon-fiber with high graphitization.

## References

- 1 J. M. Tarascon and M. Armand, *Nature*, 2001, **414**, 359–367.
- 2 K. Ariyoshi and T. Ohzuku, *J. Power Sources*, 2007, **174**, 1258–1262.
- 3 X. Zeng, M. Li, D. Abd El-Hady, W. Alshitari, A. S. Al-Bogami, J. Lu and K. Amine, *Adv. Energy Mater.*, 2019, **9**, 1900161.
- 4 F. Wu, J. Maier and Y. Yu, *Chem. Soc. Rev.*, 2020, **49**, 1569–1614.
- 5 T. Waldmann, S. Rössler, M. Blessing, R. Schäfer, R.-G. Scurtu, W. Braunwarth and M. Wohlfahrt-Mehrens, *J. Electrochem. Soc.*, 2021, **168**, 090519.
- 6 T. Ohzuku, A. Ueda and M. Nagayama, *J. Electrochem. Soc.*, 1993, **140**, 1862–1870.
- 7 C. Delmas, M. Ménétrier, L. Croguennec, I. Saadoun, A. Rougier, C. Poullier, G. Prado, M. Grüne and L. Fournès, *Electrochim. Acta*, 1999, **45**, 243–253.
- 8 T. Ohzuku, K. Ariyoshi, Y. Makimura, N. Yabuuchi and K. Sawai, *Electrochemistry*, 2005, **73**, 2–11.
- 9 Y. K. Sun, S. T. Myung, B. C. Park, J. Prakash, I. Belharouak and K. Amine, *Nat. Mater.*, 2009, **8**, 320–324.
- 10 W. Liu, P. Oh, X. Liu, M. J. Lee, W. Cho, S. Chae, Y. Kim and J. Cho, *Angew. Chem., Int. Ed.*, 2015, **54**, 4440–4457.
- 11 J. Xu, F. Lin, M. M. Doeff and W. Tong, *J. Mater. Chem. A*, 2017, **5**, 874–901.
- 12 M. Bianchini, M. Roca-Ayats, P. Hartmann, T. Brezesinski and J. Janek, *Angew. Chem., Int. Ed.*, 2019, **58**, 10434–10458.
- 13 M. M. Thackeray, S.-H. Kang, C. S. Johnson, J. T. Vaughey, R. Benedek and S. A. Hackney, *J. Mater. Chem.*, 2007, **17**, 3112–3125.
- 14 J. B. Goodenough and Y. Kim, *Chem. Mater.*, 2010, **22**, 587–603.
- 15 T. Ohzuku, M. Nagayama, K. Tsuji and K. Ariyoshi, *J. Mater. Chem.*, 2011, **21**, 10179–10188.
- 16 A. Grimaud, W. T. Hong, Y. Shao-Horn and J. M. Tarascon, *Nat. Mater.*, 2016, **15**, 121–126.
- 17 G. Assat and J.-M. Tarascon, *Nat. Energy*, 2018, **3**, 373–386.
- 18 K. Ariyoshi, Y. Orikasa, K. Kajikawa and Y. Yamada, *J. Mater. Chem. A*, 2019, **7**, 13641–13649.
- 19 Y. Mahara, N. Nagasako, H. Oka, Y. Kondo, S. Kosaka, H. Nakano, T. Nonaka and Y. Makimura, *ACS Appl. Mater. Interfaces*, 2022, **14**, 24321–24331.
- 20 N. Yabuuchi, *Curr. Opin. Electrochem.*, 2022, **34**, 100978.
- 21 M. Zhang, D. A. Kitchaev, Z. Lebens-Higgins, J. Vinckeviciute, M. Zuba, P. J. Reeves, C. P. Grey, M. S. Whittingham, L. F. Piper and A. Van Der Ven, *Nat. Rev. Mater.*, 2022, **7**, 522–540.
- 22 Y. Sun, N. Liu and Y. Cui, *Nat. Energy*, 2016, **1**, 16071.
- 23 D. Lin, Y. Liu and Y. Cui, *Nat. Nanotechnol.*, 2017, **12**, 194–206.
- 24 K. Feng, M. Li, W. Liu, A. G. Kashkooli, X. Xiao, M. Cai and Z. Chen, *Small*, 2018, **14**, 1702737.
- 25 K. Sun, T. S. Wei, B. Y. Ahn, J. Y. Seo, S. J. Dillon and J. A. Lewis, *Adv. Mater.*, 2013, **25**, 4539–4543.
- 26 H. Sun, J. Zhu, D. Baumann, L. Peng, Y. Xu, I. Shakir, Y. Huang and X. Duan, *Nat. Rev. Mater.*, 2018, **4**, 45–60.
- 27 L. Lu, Y. Hu and K. Dai, *Mater. Today Chem.*, 2017, **5**, 24–33.
- 28 H. Qu, X. Lu and M. Skorobogatiy, *J. Electrochem. Soc.*, 2018, **165**, A688–A695.
- 29 A. Yadav, B. De, S. K. Singh, P. Sinha and K. K. Kar, *ACS Appl. Mater. Interfaces*, 2019, **11**, 7974–7980.
- 30 Y. Zhou, C. H. Wang, W. Lu and L. Dai, *Adv. Mater.*, 2020, **32**, 1902779.
- 31 F. Mo, G. Liang, Z. Huang, H. Li, D. Wang and C. Zhi, *Adv. Mater.*, 2020, **32**, 1902151.
- 32 J. He, C. Lu, H. Jiang, F. Han, X. Shi, J. Wu, L. Wang, T. Chen, J. Wang, Y. Zhang, H. Yang, G. Zhang, X. Sun, B. Wang, P. Chen, Y. Wang, Y. Xia and H. Peng, *Nature*, 2021, **597**, 57–63.
- 33 S. Ling, X. Li, T. Zhou, R. Yuan, S. Sun, H. He and C. Zhang, *Adv. Mater.*, 2023, **35**, 2211201.
- 34 L. E. Asp, M. Johansson, G. Lindbergh, J. Xu and D. Zenkert, *Funct. Compos. Struct.*, 2019, **1**, 042001.
- 35 A. M. Stephan, *Eur. Polym. J.*, 2006, **42**, 21–42.
- 36 E. Jacques, M. H. Kjell, D. Zenkert and G. Lindbergh, *Carbon*, 2014, **68**, 725–733.



- 37 A. P. Nowak, J. Hagberg, S. Leijonmarck, H. Schweinebarth, D. Baker, A. Uhlin, P. Tomani and G. Lindbergh, *Holzforschung*, 2018, **72**, 81–90.
- 38 B. Huang, Z. Pan, X. Su and L. An, *J. Power Sources*, 2018, **399**, 274–286.
- 39 M. Ender, A. Weber and E. Ivers-Tiffée, *Electrochem. Commun.*, 2013, **34**, 130–133.
- 40 Y. Nomura, I. V. Anoshkin, C. Okuda, M. Iijima, Y. Ukyo, H. Kamiya, A. G. Nasibulin and E. I. Kauppinen, *J. Nanomater.*, 2014, **2014**, 586241.
- 41 I. Miccoli, F. Edler, H. Pfnur and C. Tegenkamp, *J. Phys.: Condens. Matter*, 2015, **27**, 223201.
- 42 T. Ohzuku, Y. Iwakoshi and K. Sawai, *J. Electrochem. Soc.*, 1993, **140**, 2490–2498.
- 43 J. R. Dahn, T. Zheng, Y. Liu and J. S. Xue, *Science*, 1995, **270**, 590–593.
- 44 R. Mead-Hunter, A. J. King and B. J. Mullins, *Langmuir*, 2012, **28**, 6731–6735.
- 45 W. Bauer and D. Nötzl, *Ceram. Int.*, 2014, **40**, 4591–4598.
- 46 P. Wang, J. Zhou, B. Xu, C. Lu, Q. Meng and H. Liu, *Adv. Mater.*, 2020, **32**, 2003453.
- 47 K. Naito, J.-M. Yang, Y. Xu and Y. Kagawa, *Carbon*, 2010, **48**, 1849–1857.
- 48 T. M. M. Heenan, A. Jnawali, M. D. R. Kok, T. G. Tranter, C. Tan, A. Dimitrijevic, R. Jervis, D. J. L. Brett and P. R. Shearing, *J. Electrochem. Soc.*, 2020, **167**, 140530.
- 49 M. Scheller, A. Aufschläger, A. Frank, M. Steinhardt, J. Sturm and A. Jossen, *J. Energy Storage*, 2022, **56**, 105942.
- 50 S. Picard, D. T. Burns and P. Roger, *Metrologia*, 2007, **44**, 294–302.
- 51 K. E. Thomas, J. Newman and R. M. Darling, *Mathematical modeling of lithium batteries*, Springer, 2002.
- 52 S. Santhanagopalan, P. Ramadass and J. Zhang, *J. Power Sources*, 2009, **194**, 550–557.
- 53 L. Cai and R. E. White, *J. Power Sources*, 2011, **196**, 5985–5989.
- 54 R. H. P. Liang, T. Zou, K. Somasundaram, W. Tong and E. Birgersson, *J. Electrochem. Sci. Eng.*, 2014, **4**, 1–17.
- 55 P. Priimägi, H. Kasemägi, A. Aabloo, D. Brandell and V. Zadin, *Electrochim. Acta*, 2017, **244**, 129–138.
- 56 X. Feng, X. He, L. Lu and M. Ouyang, *J. Electrochem. Soc.*, 2018, **165**, A155–A167.

